Three-Dimensional Rotation of Mouse Embryos

Clement Leung, *Student Member, IEEE*, Zhe Lu, *Member, IEEE*, Xuping P. Zhang, *Member, IEEE*, and Yu Sun*, *Senior Member, IEEE*

***Abstract*—Research and clinical applications, such as microinjection and polar-body biopsy involve 3-D rotation of mammalian oocytes/embryos. In these cell manipulation tasks, the polar body of an embryo/oocyte must be made visible and properly oriented under optical microscopy. Cell rotation in conventional manual operation by skilled professionals is based on trial and error, such as through repeated vacuum aspiration and release. The randomness of this manual procedure, its poor reproducibility, and inconsistency across operators entail a systematic technique for automated, noninvasive, 3-D rotational control of single cells. This paper reports a system that tracks the polar body of mouse embryos in real time and controls multiple motion control devices to conduct automated 3-D rotational control of mouse embryos. Experimental results demonstrated the system's capability for polar-body orientation with a high success rate of 90%, an accuracy of 1.9°, and an average speed of 22.8 s/cell (versus averagely 40 s/cell in manual operation).**

***Index Terms*—Automation, cell manipulation, cell orientation, cell recognition, cell rotation, cell tracking, embryos, oocytes, polar body, 3-D, visual servo.**

I. Introduction

CELLULAR surgery demands a range of techniques for manipulating single cells. Cell injection and intracellular structure biopsy are example techniques practiced in genetics studies and stem cell research as well as clinical *in vitro* fertilization procedures. These cellular surgery techniques target specific cellular structures, requiring cells to be noninvasively rotated in three dimensions for properly orienting target cellular structures for manipulation.

In intracytoplasmic sperm injection (ICSI), the polar body of the oocyte must be oriented away from the micropipette penetration site to preserve the cell's development competence [1]–[4]. Cell orientation is also critical for biopsy of cellular structures. In preimplantation genetic diagnosis (PGD), polar-body biopsy is widely practiced [5] for genetic screening of the embryo before implantation [6]. The polar body (see Fig. 1) is a structure that contains a copy of the genetic information of the oocyte/embryo, and thus, can be extracted to analyze the embryo for genetic defects. Polar-body biopsy requires the polar body to be properly rotated for extraction by a biopsy micropipette.

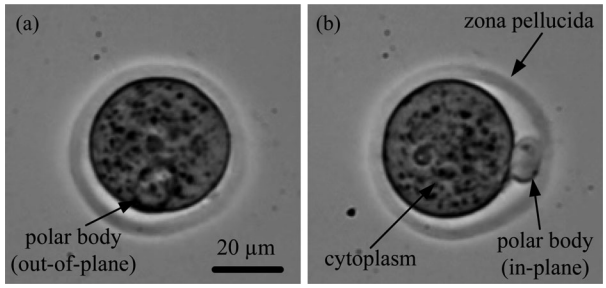

Fig. 1. Polar body of an oocyte/embryo must be properly oriented for applications such as ICSI and PGD polar-body biopsy. Orienting the polar body is a 3-D task. (a) Mouse embryo with polar body on a different depth than the image plane (out of plane). (b) Mouse embryo with polar body fully in the image plane (in plane).

Cell rotation in these research and clinical applications has been conventionally performed manually by skilled operators. The operator uses a micropipette to repeatedly apply vacuum and release of the cell until the targeted cellular structure becomes visible and is properly oriented. Due to poor controllability, manual 3-D rotation of cells is a trial-and-error procedure [1] that varies in speed and success rates across operators. With the trend of automating cell manipulation tasks [7]–[13], an automated approach is required for well controlled 3-D rotation of biological cells with high reproducibility and success rates.

A number of approaches have been reported in the literature for rotating single cells. Optical tweezers use a focused laser beam to manipulate microscopic objects and are capable of orienting single cells [14]–[18]. However, the optical tweezers technique is limited to rotating a cell about one axis [19]. Dielectrophoresis (DEP) uses a nonuniform electric field to exert forces on cells and has been shown capable of rotating cells [20]–[23]. It has also been shown that the electric fields required for DEP to rotate cells can cause significant cell damage [24]. Strong static magnetic fields can also be used to orient cells [25], [26]; however, cell orientation is limited to the alignment with the magnetic field direction. We recently reported a customized rotational stage design and control approaches for orienting cellular structures [27]. The system and technique were limited to orienting cells about only one axis (i.e., 2-D orientation).

The aforementioned methods are not suitable for applications such as ICSI and PGD, which require noninvasive 3-D rotation of single mammalian oocytes/embryos. To establish an automated technique for orienting targeted cellular structures, visual recognition and tracking algorithms are essential for locating and following the position of the cellular structures imaged under microscopy. Since microscope images are 2-D,

Manuscript recieved August 9, 2011; revised December 6, 2011; accepted December 21, 2011. Date of publication January 5, 2012; date of current version March 21, 2012. This work was supported by the Natural Sciences and Engineering Research Council of Canada, the Canada Research Chairs Program, and the Ontario Genomics Institute. *Asterisk indicates corresponding author*.

C. Leung, Z. Lu, and X. P. Zhang are with the Advanced Micro and Nanosystems Laboratory, University of Toronto, Toronto, ON M5S 3G8, Canada (e-mail: clement.leung@utoronto.ca; zhe.lu@utoronto.ca; zhxp@mie.utoronto.ca).

*Y. Sun is with the Advanced Micro and Nanosystems Laboratory, University of Toronto, Toronto, ON M5S 3G8, Canada (e-mail: sun@mie.utoronto.ca).

Color versions of one or more of the figures in this paper are available online at http://ieeexplore.ieee.org.

Digital Object Identifier 10.1109/TBME.2012.2182995

targeted cellular structures may rotate out of the image plane of the microscope when the cell is rotated along three dimensions. Thus, targeted cellular structures to manipulate are not always visible. Furthermore, other cellular structures tend to occlude the cellular structure of interest, rendering focus-based approaches ineffective for recovering the visibility of the desired cell structure. In light of these challenges, robust cellular structure recognition and tracking algorithms are required to accomplish 3-D rotation of targeted cellular structures. With visual feedback of the cellular structure position, a fluidic flow can be controlled for cell rotation to produce a torque that rotates a cell (e.g., oocyte/embryo). A fluidic flow has two main regions: a laminar flow region, where fluid motion is smooth and constant [28], and a turbulent flow region, characterized by chaotic eddies, vortices, and other flow instabilities [29]. For stable cell rotation, the laminar flow region needs to be maximized by controlling the fluidic flow rate.

This paper presents a system and techniques for automated 3-D rotational control of single mammalian oocytes/embryos. The system was applied to the positioning and orientation of the polar body of mouse oocytes/embryos. A robust polar-body recognition algorithm, which is capable of determining whether the polar body is present in the image plane of the microscope (in plane) or on a different plane/depth from the image plane (out of plane), was developed. Furthermore, a robust polar-body tracking algorithm was developed for tracking the polar body while it was rotated. Different from the rotational stage approach [27], this system does not require customized hardware controlling cell rotation. The system uses a standard holding micropipette to generate a fluidic flow to rotate the polar body from an out-of-plane position to an in-plane position, and then to rotate the polar body to a desired orientation in the image plane. Visual recognition and tracking of the polar body is combined with motion control to automatically control the fluid flow generated by a holding micropipette to rotate the polar body. The system provides a noncontact, noninvasive, and highly reproducible approach for automatically rotating cellular structures in three dimensions.

II. System Design

A. System Setup

As shown in Fig. 2, the system consists of a standard inverted microscope (bright-field imaging, Nikon Ti–S), a CMOS camera (scA1300-32gm, Basler), and a motorized X–Y translational stage (ProScan, Prior Scientific, Inc.) for embryo positioning control. The stage has a travel range of 75 mm with a resolution of 0.01 μm, a maximum speed of 5 mm/s, and a repeatability of ± 1 μm. A $10\times$ objective with a numerical aperture of 0.30 (CFI Plan Fluor, Nikon) was used for imaging.

A standard holding micropipette (Cook; tip diameter: 15 μm, tilting angle: 35°) is connected to a 250 μL glass syringe (Hamilton). The syringe was filled with mineral oil and mounted on a linear stage (eTrack, Newmark System, Inc.) for precise pL control of fluid to generate fluidic flow for cell rotational control. The holding micropipette was attached to a three-axis motorized micromanipulator (MP285, Sutter, Inc.). The micromanipulator has a travel range of 25 mm and a resolution of 0.04 μm. A host computer controls all motion control devices (X–Y motorized stage, micromanipulator, and linear stage) and processes images in real time (30 Hz).

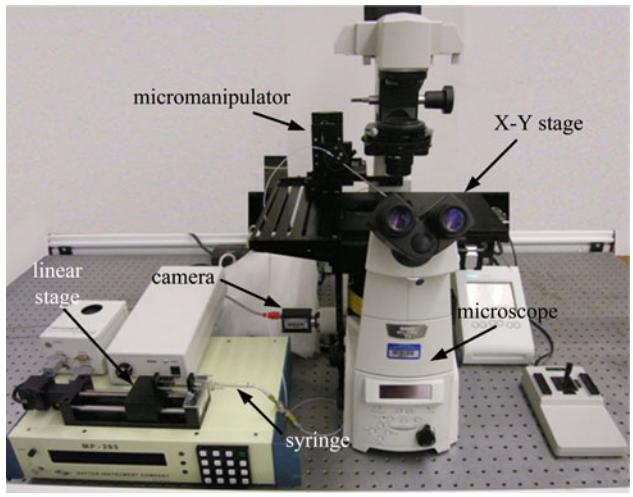

Fig. 2. Cell manipulation system setup.

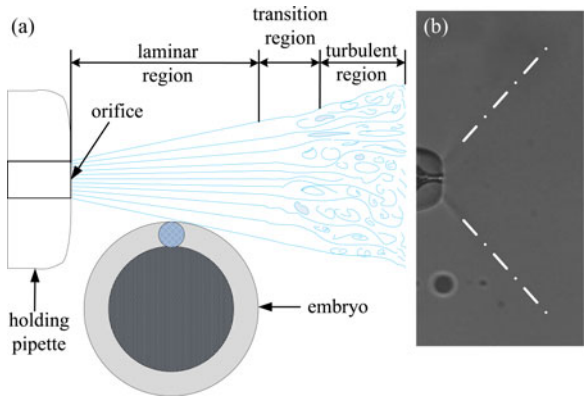

Fig. 3. Analysis of fluidic flow produced by holding micropipette. (a) Schematic illustration of different flow regions. (b) Experimental visualization of the laminar flow region. Dark lines represent the laminar flow region as colored dyes were dispensed. The white dotted lines illustrate the extension of the laminar flow region.

B. Analysis of Fluidic Flow

Aspiration and dispensation of fluid from the holding micropipette is controlled by displacements from the linear stage. Positive and negative linear stage displacements cause the micropipette to dispense fluid or aspirate fluid. Fluidic flow is used to produce a torque that rotates the embryo and its polar body. Laminar flow and turbulent flow can be generated by the holding micropipette [see Fig. 3(a)]. Laminar flow is characterized by smooth and constant fluid motion, which is ideal for stable rotation of cells. In contrast, turbulent flow generates chaotic eddies, vortices, and other flow instabilities. In order to achieve stable cell rotational control, the micropipette must be positioned relatively close to the cell for ensuring that the cell is only rotated within the laminar flow region.

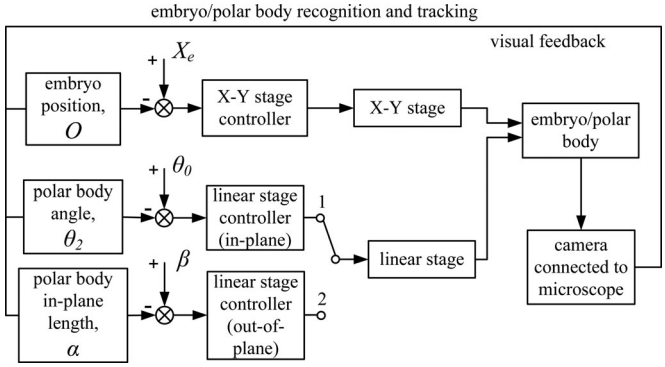

Fig. 4. Control architecture of the system. Motion control devices include an X–Y motorized stage and a linear stage for controlling fluidic flow. Switch 1 is for in-plane rotational control. Switch 2 is for out-of-plane rotational control. X_e is the center region of the field of view. θ_0 is the desired orientation of the polar body. β is a threshold value at which the polar body is determined to be in the image plane.

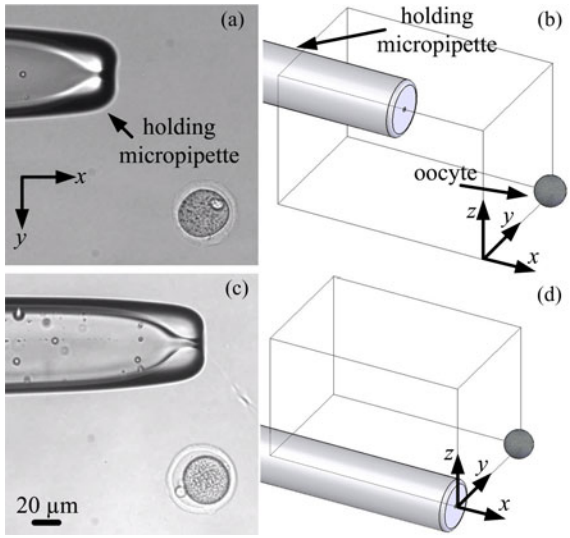

Fig. 5. (a) Micropipette positioning for out-of-plane rotational control. (b) 3-D schematic of micropipette positioning for out-of-plane rotational control. (c) Micropipette positioning for in-plane rotational control. (d) 3-D schematic of micropipette positioning for in-plane rotational control.

Flow rates generated by the micropipette affect the size of the laminar and turbulent flow regions. Lower flow rates result in a larger laminar flow region. Thus, to further ensure that the cell is within the laminar flow region, the size of the laminar flow region can be maintained large by limiting the linear stage displacement rate. To visually analyze the laminar flow region, colored dyes were dispensed from the holding micropipette into culture medium [see Fig. 3(b)]. We experimentally determined that ± 5 μm/s was the minimum and maximum linear stage velocity used by our system to produce a sufficiently large laminar flow region. Through experimental trials on rotating embryos with a constant linear stage velocity between -5 and 5 μm/s, we determined that aspiration and dispensation at the same flow rate achieved the same stable rotational control of cells. Thus, controllable size of the laminar flow region is similar for both aspiration and dispensation at these linear stage velocities.

C. Operation Sequence for Cell Rotational Control

When an embryo of interest is selected, the system starts to track the embryo and provide visual feedback of the embryo's position O to the X–Y stage controller. Determination of the embryo's position enables the X–Y stage to move the embryo to the center of the field of view of the microscope, X_e (see Fig. 4) in each frame to compensate for the embryo's translational movement during rotation. The spatial distance between the embryo's position and the center of the field of view is input into a controller to servo the X–Y stage to maintain the embryo in the center of the field of view.

Polar-body recognition is performed to determine if the polar body is out of plane or in plane. If no polar body is found, or if the polar body is not sufficiently present in the image plane, the micropipette tip is translated to a vertical distance above the embryo, and to the top left-hand side of the embryo for out-of-plane rotation [e.g., micropipette tip position relative to cell $(x, y, z) = (-60, 100, 30$ μm)] [see Fig. 5(a)]. In out-of-plane rotational control, the linear stage is visually servoed to generate fluidic flow. The fluidic flow produces a torque that rotates the polar body about the image plane (xy plane) until the polar body is detected by the recognition algorithm to be sufficiently present in the image plane. If no polar body is found after 30 s, the system determines that the embryo does not have a polar body, and polar-body rotation is stopped.

Once the polar body is sufficiently present in the image plane, polar-body tracking commences for in-plane rotational control. The holding micropipette is positioned back in the image plane and translated relatively to the embryo such that the embryo is within the laminar flow region [e.g., micropipette tip position $(x, y, z) = (0, 100,$ and $0)$] [see Fig. 5(b)]. The micromanipulator moves at a low speed (e.g., 20 μm/s) to ensure that the micropipette's movement does not cause disturbances in the medium that could potentially change the cell's in-plane orientation. The polar-body position is continuously tracked during in-plane rotation and used to visually servo the linear stage to rotate the polar body to the target orientation (e.g., 3 o'clock or 12 o'clock position, labeled as θ_0 in Fig. 4). The embryo is then immobilized in the desired orientation for subsequent cellular surgery (e.g., microinjection or polar-body PGD).

III. Polar-Body Recognition

The polar-body recognition algorithm locates the initial position of the polar body at the start of the system. If the polar body is detected to be in the image plane, the system directly performs in-plane rotation. Otherwise, out-of-plane rotation is first conducted to bring the polar body into the image plane.

A. Segmentation of Embryo Structures

The system first applies Otsu adaptive thresholding to form a binary image of the embryo. A morphological close operation (dilation and erosion of the binary image) is performed to remove noise and small particles that may be present in the image [see Fig. 6(b)] [30]. To detect the polar body in the binary

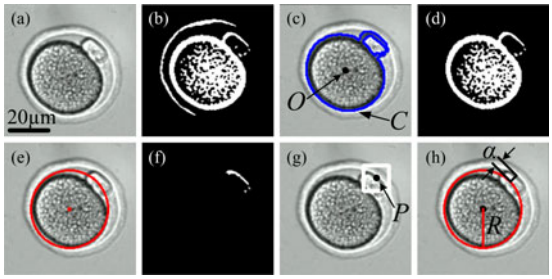

Fig. 6. Image-processing sequence conducted for polar-body recognition and tracking. (a) Original image. (b) Binary image. (c) Cytoplasm and polar-body contour C. (d) Binary image after removal of zona pellucida. (e) Fitted cytoplasm circle (red). (f) Binary image after removal of cytoplasm. (g) pbROI, shown by the white box, is centered at the located polar-body position P. (h) Determination of the length of polar body α in image plane.

image, all other components of the embryo, such as the zona pellucida and the cytoplasm, are removed from the binary image. The embryo's position O [see Fig. 6(c)] is found by computing C, which is the contour formed by the cytoplasm and the polar body, and then computing the centroid of C. Removal of non-polar body binary objects is accomplished by using the contour C, to segment the cytoplasm and polar body from the rest of the image [see Fig. 6(d)].

The algorithm then removes the cytoplasm from the binary image. Since cytoplasm is approximately circular in shape, a circle is fitted to the binary information of the cytoplasm to segment the cytoplasm from the binary image [see Fig. 6(e)]. The Euclidean norm between O and each contour point in C is first computed. The mode Euclidean norm value is taken to be the radius R of the circle fitted to the cytoplasm, with O as the circle's center. Cytoplasm binary information is then removed from the binary image [see Fig. 6(f)].

B. Polar-body Detection

The polar body's position is computed by finding the contours of the remained binary objects. There may be multiple contours since the binary information representing the polar body can be fragmented [see Fig. 6(f)]. Furthermore, there are cases where the cytoplasm's fitted circle may not have encapsulated the entire cytoplasm. Consequently, edges of the cytoplasm can remain in the binary image. However, this tends to happen mostly for unhealthy deteriorating embryos, where the cytoplasm has an altered morphology.

In order to correctly find the polar body, the width of each contour is extracted to distinguish the polar body from potential cytoplasm edges. Each binary object's contour width is computed by finding the two contour points of the binary object that produce the maximum Euclidean norm value. Experimentally, the width of a polar body is always lower than 30 pixels, verified through off-line measurements on many mouse embryos. On the other hand, cytoplasm edge binary objects generally have widths much higher than 30 pixels. This experimental knowledge provides a useful cue/threshold for identifying the polar body. After the polar body is detected, the polar body position is extracted by finding the centroid of the maximum area contour that meets the aforementioned polar body width requirement. The system then forms a polar-body region of interest (pbROI) around the centroid position P [see Fig. 6(g)].

C. Length of Polar-body In Plane

The system then determines the amount of polar body that is in the image plane by determining the polar-body length α (in pixels) [see Fig. 6(h)]. Based on the cytoplasm radius R, and the distance between the polar body and O, the difference is used to measure the length of the polar body, α that is present in the image plane. The polar-body distance from O is found by calculating the difference between the point on the polar body that produces the largest distance from the cytoplasm center O. β, measured in pixels, is a threshold value at which the polar body is determined to be in the image plane. It was experimentally found that α always exceeds 6 pixels when the polar body is in the image plane and, thus, $\beta = 6$ was set in the system as the minimum length requirement for determining if the majority of the polar-body structure is within the microscope image plane.

The variable α together with the threshold value β is used by the out-of-plane controller to control the linear stage for out-of-plane rotation (see Fig. 4), which will be discussed in more detail in Section IV. If the polar body was not detected during polar-body detection, then the polar body is considered to be completely out of plane, and α is set to 0. If the minimum α requirement is met, the system directly executes in-plane rotation. However, if this requirement is not met, or if the polar body is not detected, the system first conducts out-of-plane rotation to rotate the polar body into the image plane before performing in-plane rotation.

IV. Out-of-Plane Rotational Control

Out-of-plane rotational control is required when the polar body is not detected, or when the minimum α threshold requirement is not met. The polar body must be rotated about the x- and y-axis until the polar body becomes sufficiently present in the image plane.

To conduct out-of-plane rotational control, the micromanipulator moves the holding micropipette to an out-of-plane position [see Fig. 5(a)]. The micropipette applies fluidic flow predominantly to the top part of the embryo, thus, causing the embryo to rotate about the xy plane. The α value is input into a piecewise controller to visually servo the linear stage for out of plane polar-body rotation (see Fig. 4). The piecewise controller switches among several control states based on α. In (1), d represents the linear stage velocity and i represents the current image frame. When α is 0 [i.e., when the polar body is completely out of plane, Fig. 7(a)], the polar body is rotated at a constant rate. When α becomes greater than 0 but less than β, the system switches to proportional control with a gain of kp_1.

$$d = \begin{cases} 1\ \mu\text{m/s}, & \text{if } \alpha = 0 \\ kp_1(\alpha - \beta), & \text{if } 0 < \alpha \leq \beta \\ 0, & \text{if } \alpha > \beta, \alpha(i-1) < \alpha(i) \\ -1\ \mu\text{m/s}, & \text{if } \alpha > \beta, \alpha(i-1) \geq \alpha(i). \end{cases} \quad (1)$$

The kp_1 value was set at 0.000085 in the system, tuned through experimental trials. A minimum threshold of -1 μm/s and a

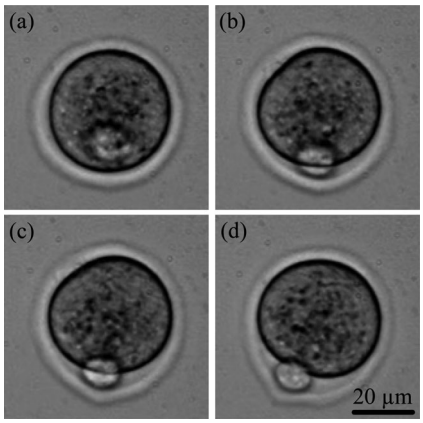

Fig. 7. Out-of-plane rotation. (a) Initial position of the polar body is on a different plane from the image plane (out of plane). (b–c) Polar body is partially in plane as the polar body is rotated into the image plane. (d) Polar body is completely in the image plane, ready for in-plane rotation to the target orientation.

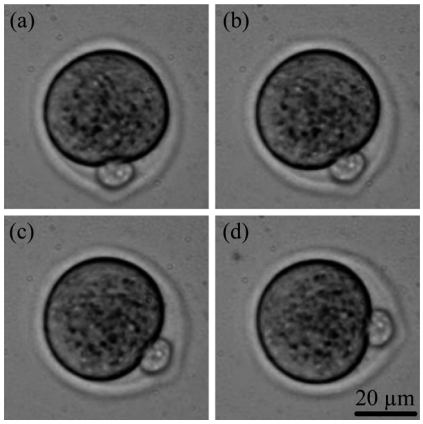

Fig. 8. In-plane rotation. (a) Polar body is in the microscope's image plane (in plane). (b–c) Polar body is rotated in-plane counterclockwise. (d) In-plane rotation stops, as polar body reaches the 3 o'clock ($\theta_0 = 0$) destination position and orientation.

maximum threshold of 1 μm/s were set to d to ensure that a low-fluidic flow rate is generated by the micropipette for stable rotation of the embryo/polar body. Furthermore, these thresholds restrict the allowable linear stage velocity to a very small range of low velocities. Thus, the acceleration of the linear stage is limited, ensuring a smooth transition with no abrupt changes in the linear stage's velocity between different control states. When α exceeds β, the system stops the linear stage from moving until α is observed to decrease between consecutive frames. This happens when the polar body has reached its maximum α value and begins to rotate out of the image plane again. The system then applies a negative linear stage displacement of -1 μm/s to compensate for the decrease in α value.

After a number of consecutive frames (e.g., 60 frames or 2 s) of maintaining the polar body's α length at a value greater than or equal to β, the polar body is considered to be in plane, and out-of-plane rotational control is completed. If after 30 s of out-of-plane rotation, α remains at 0, the system stops out-of-plane rotation, since a low number of embryos indeed do not have a polar body.

V. In-Plane Rotational Control

When the polar body is within the image plane, the system initiates in-plane rotational control of the cell (Fig. 8). Similar to out-of-plane rotational control, the micromanipulator is moved at a slow velocity (e.g., 20 μm/s) to position the micropipette at the in-plane rotation position [see Fig. 5(b)]. At this position, the micropipette tip is on the same Z depth as the embryo, enabling the fluidic flow from the micropipette to rotate the embryo about the Z-axis. The micropipette is positioned away from the embryo in the y-direction, by slightly more than one embryo size to minimize the chance of aspirating the embryo onto the micropipette tip opening. A visual tracking algorithm was developed to track the polar body in the rotation process. The tracked position of the polar body is used to visually servo the linear stage to rotate the polar body in plane to a target orientation (e.g., 3 o'clock position).

A. Polar-body Visual Tracking

The initial position of the polar body is determined through polar-body recognition described in Section III. To track the polar body, optical flow is used to extract the 2-D motion field of the embryo and polar body's in-plane rotation. With the optical flow method, corner detection is performed on previous image frame $i-1$ to compute feature points to track. The locations of these feature points are then found in the current frame i to form the motion field vectors, based on which the direction of rotation (counterclockwise or clockwise) and the rotation angle θ_1 are extracted.

The information of θ_1 is computed by first subtracting the coordinates O from each feature point coordinate in frame $i-1$ and frame i to form $\mathbf{f}_j(i-1)$ and $\mathbf{f}_j(i)$, respectively, where j corresponds to the number of feature points, and $\mathbf{f}_j(i)$ and $\mathbf{f}_j(i-1)$ are feature point positions relative to O. To find the angle of rotation θ_1, the dot product of each $\mathbf{f}_j(i-1)$ and $\mathbf{f}_j(i)$ pair is computed and averaged:

$$\theta_1 = \frac{1}{N}\sum_{j=0}^{N} \arccos \frac{\mathbf{f}_j(i-1)\cdot \mathbf{f}_j(i)}{\|\mathbf{f}_j(i-1)\|\|\mathbf{f}_j(i)\|} \tag{2}$$

The cross product of $\mathbf{f}_j(i-1)$ and $\mathbf{f}_j(i)$ for every corresponding j pair is also computed and summed to find the rotational direction about the Z-axis. A negative summation result represents that the polar body and embryo are rotating in a counterclockwise direction, and a positive summation result represents that the embryo and polar body are rotating in a clockwise direction.

The rotation angle θ_1 is multiplied by the rotation direction, and is then input into a rotational matrix to rotate the previous frame's polar-body position by θ_1. O is subtracted from the polar-body position in the previous frame $P(i-1)$ to find the polar-body vector $\mathbf{p}(\mathbf{i}-\mathbf{1})$, which is then multiplied by a rotation matrix with value θ_1 to determine the current frame's $\mathbf{p}(\mathbf{i})$:

$$\mathbf{p}(\mathbf{i}) = \begin{bmatrix} \cos\theta_1 & -\sin\theta_1 \\ \sin\theta_1 & \cos\theta_1 \end{bmatrix} \mathbf{p}(\mathbf{i}-\mathbf{1}). \tag{3}$$

O is added to the newly updated $\mathbf{p}$ to compute the polar-body position P. To verify that a polar body exists at the newly estimated P position, the polar-body binary information is extracted from the current frame using the polar-body detection method described in Section III. A pbROI is formed and centered at the estimated P position. If sufficient polar-body binary information is found in pbROI, P is updated to be centered at the centroid of the polar-body binary contour. Otherwise, no polar body exists at the newly computed location, and the algorithm continues to estimate the next position of the polar body based on the optical flow vectors.

It was mentioned earlier that embryo structures of a low number of healthy embryos and mostly deteriorating embryos are no longer uniform. The nonuniformity of the embryo can cause minor out-of-plane rotation when the embryo is rotated in plane, where the polar body would disappear from the image plane for a short period of time, and then reappear. If polar-body tracking does not recover the polar-body location (i.e., polar body does not reappear) after several seconds, in-plane rotation is stopped, and the system switches back to out-of-plane rotation to bring the polar body back into the image plane.

B. Visual Servo Control

The angle of the polar-body θ_2, relative to the target orientation (e.g., 3 o'clock position) is input into a potential difference (PD) controller to visually servo the linear stage for in-plane rotation (see Fig. 4). θ_2 is extracted from $\mathbf{p}$. The PD controller is represented as

$$d = kp_2(\theta_2 - 0) + kd_2(0 - \theta_1') \tag{4}$$

where θ_1' is the angular velocity of the polar body in degree/s, and kp_2 and kd_2 are the proportional and derivative gains, respectively. Starting values of proportional and derivative gains were obtained using standard methods [31], and their final values were determined through experimental trials. kp_2 and kd_2 were set to be 0.00018 and 0.003. Angular velocity is computed by averaging the rotational angle θ_1 of the current frame i and the past 29 frames.

The controller's output d is capped at a maximum threshold of 5 μm/s and a minimum threshold of -5 μm/s. The thresholds limit the linear stage displacement to ensure that the embryo is not aspirated onto the micropipette tip opening. Furthermore, these limits ensure that a sufficiently large laminar flow region is produced so that the polar body is rotated stably.

VI. Experimental Results and Discussion

Mouse embryos collected from imprinting control region mice were placed in culture medium in a petri dish. The culture medium was covered with mineral oil to prevent culture medium evaporation. A total of 30 mouse embryos were used to capture 30 off-line videos for evaluating the recognition and tracking algorithms. The system's out-of-plane and in-plane rotational control performances were evaluated separately, using additionally 30 mouse embryos.

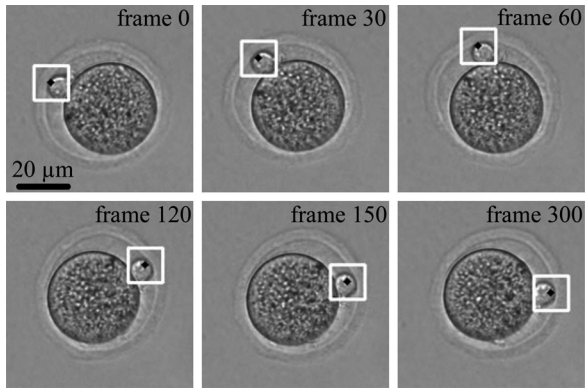

Fig. 9. Polar body being tracked and rotated clockwise to the 3 o'clock orientation.

A. Polar-body Recognition and Tracking

Polar-body recognition and tracking success rates were evaluated by running the algorithms on the 30 off-line captured videos of mouse embryos rotated by manually controlling fluidic flow. The videos were captured at a frequency of 30 frames/s using $10\times$ magnification under bright field microscopy. The embryos were rotated by controlling the fluidic flow manually, decoupling the control of the fluidic flow from the evaluation of the recognition and tracking algorithms.

1) Recognition Success Rate: Recognition success rate is defined as the ability of the algorithm to automatically detect the polar body when the polar body is partially or fully present in the image plane. The recognition algorithm achieved a recognition success rate of 93% (28 out of 30). False-positive recognition occurred when contaminants in culture medium were very occasionally present close to the polar body. When the contaminants passed the polar body width criterion described in Section III-B, they were incorrectly detected as the polar body. This failure rate can be reduced by ensuring that culture medium is filtered and that no contaminants are attached to the embryos.

2) In-Plane Tracking Success Rate: The 30 off-line captured videos containing in-plane rotation of mouse embryos and their polar bodies were used to evaluate the polar-body tracking algorithm. The videos have an average duration of 54 s. Tracking success rate is defined as the ability of the algorithm to follow the polar body throughout the duration of the off-line videos. Failure happens when the tracking algorithm loses track of the polar body in a given video. Based on the 30 videos, the algorithm's polar-body tracking success rate was evaluated to be 97% (i.e., the tracking algorithm did not lose track of the polar body in 29 out of 30 of the videos). Fig. 9 shows example frames of polar-body tracking during in-plane rotation. The pbROI is labeled as white boxes, and the polar-body position P is shown by the dot located at the center of the pbROI. One failure case occurred when the embryo's polar body had a low contrast relative to the background. The algorithm determined that the polar body was lost, and after several seconds the system automatically canceled tracking.

B. Out-of-Plane Rotational Control

For out-of-plane rotational control, the amount of time required and the success rate of the system to rotate the polar body into the image plane were both evaluated. The polar body was first manually rotated out of the image plane before conducting automated out-of-plane rotational control for cases where the polar body was partially or fully present in the image plane initially. For cases where the polar body was already out of plane, this precursor step was not necessary. Out-of-plane rotational control success rate is defined as the ability of the system to rotate and verify that the polar body is in the image plane based on the minimum α length criterion described in Section III-C. For the evaluation of the out-of-plane control, failure cases caused by polar-body recognition failure were ignored. If the polar-body recognition were to fail during an out-of-plane rotational control trial, the trial would be performed again. Thus, the out-of-plane control experimental trial results were not dependent on the recognition success rate.

Totally, 30 mouse embryos were used to perform 30 trials to quantify the system's success rate for out-of-plane rotational control. The system exhibited a success rate of 90% for out-of-plane rotation. For one of the failure cases, the polar body was abnormally small, with an α length of less than $\beta = 6$. Thus, for this case, the minimum α requirement was never met, and out-of-plane rotation was canceled by the system after 30 s. The cytoplasm shape can also cause failure to occur. For unhealthy embryos, the shape of the cytoplasm is no longer close to spherical, and has a deformed morphology. Circle fitting used to remove the cytoplasm binary information, thus, encapsulated the polar body for certain cases of unhealthy embryos. In this failure case, the polar body was rotated to the image plane, but continued to rotate out of the image plane, as the minimum α length criterion was never met.

Out of the 30 trials, the shortest and longest time required for part of the polar body to first appear in the image plane were 2 and 8 s, respectively. The average time required for the polar body to first appear partially in the image plane was 3.8 s. For successful cases only, the time required for the polar body to fully appear in the image plane after the polar body has first appeared was averagely 8.4 s. The shortest and longest duration of time from the polar body first appearing to the polar body fully appearing in the image plane were 4 and 40 s. The overall average time required for a successful out-of-plane rotation was, thus, 12.2 s. For the 40 s case, the polar body partially appeared in the image plane. However, the polar body's α value did not surpass the threshold requirement. The polar body was then rotated out of the image plane again, and then back into the image plane. The second attempt at rotating the polar body back to the image plane enabled the polar body to be fully in the image plane.

C. In-Plane Rotational Control

In-plane rotational control trials were performed by automatically rotating the polar body of each embryo to the target 3 o'clock position, defined as the 0° position. For evaluation of the in-plane rotational control, failure cases caused by tracking failure were ignored and not included in the experimental trial results. Thus, the in-plane controller was evaluated independent from the tracking algorithm success rate.

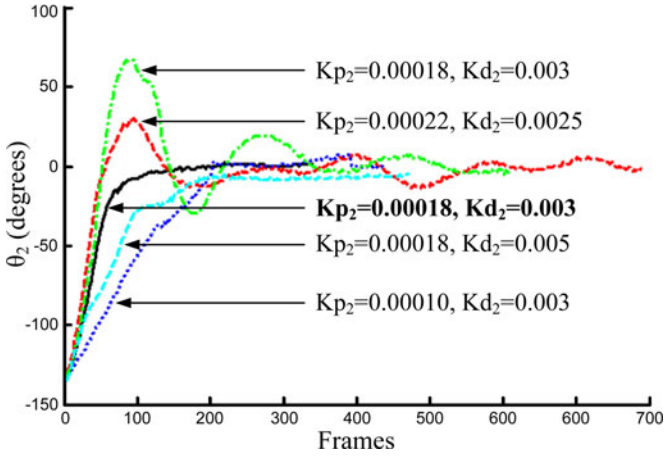

Fig. 10. Step response for different kp_2 and kd_2 values.

Each of the 30 embryos' polar bodies was rotated twice, amounting to a total number of 60 trials. One rotation was counterclockwise with the polar body starting at the 8 o'clock position (150° relative to the 3 o'clock destination position), and one rotation was clockwise with the polar body starting at the 10 o'clock position (−150° relative to the 3 o'clock destination position). The two aforementioned starting positions require two of the largest angles of rotations to reach the 3 o'clock position. Thus, trials from these two starting positions were used to quantify the response time of the in-plane controller in cases where the polar body was far away from the 3 o'clock position. The polar body was fully in the image plane before conducting the in-plane rotational control trial. As previously discussed in Section V-B, through experimental trial and error, the proportional and derivative gains for the in-plane controller were tuned to be $kp_2 = 0.00018$ and $kd_2 = 0.003$. Fig. 10 shows step responses for varying control gains.

The system required averagely 10.6 s to rotate the polar body from the initial positions to the 3 o'clock position. Correspondingly, the cell's in-plane rotational speed was observed to be approximately 13°/s. Based on these results, the overall average time required for the system to orient the polar body to the 3 o'clock position from an out-of-plane position was 22.8 s, a speed comparable to that of skilled operators. The fastest rotational speed was approximately 22°/s, enabling the system to rotate the polar body to the 3 o'clock position within 6 s. Out of the 60 trials performed on the 30 embryos, the in-plane rotational control success rate was 100%.

The rotation accuracy for the system's in-plane rotational control was evaluated by measuring the maximum angle between the desired orientation angle and the one achieved by the cell rotational control system. The final orientation angle of the polar body is computed by averaging the angles of the last 60 positions found by the polar-body tracking algorithm. Based on the 60 trials, the rotation accuracy of the system was calculated to be 1.9°. In certain cases, minor overshoot was observed,

resulting from several factors. The sizes of the embryos vary, and the difference in size can affect the rotational speed of the polar body. Slight differences in the viscosity of culture medium can also have an affect on the flow rate generated by the linear stage displacement.

Finally, undesired coupled out-of-plane rotation was very occasionally observed during in-plane rotation. It was discussed earlier that healthy embryos and deteriorating embryos reveal different rotation behavior. Due to the altered shape of unhealthy embryos, the embryo's center of mass is changed, and the polar body more readily rotates out of the image plane. Undesired out-of-plane rotation was observed in 6 out of the 60 trials.

VII. Conclusion

This paper presented a system for automated 3-D rotational control of mouse embryos. Visual recognition and tracking algorithms were developed to detect the polar body's presence or absence in the microscope's image plane and to track the polar body during in-plane rotation. Polar-body recognition and tracking success rates were quantified to be 93% and 97%, respectively. The system controls the linear stage displacement to generate fluidic flow for out-of-plane and in-plane cell rotational control. The system demonstrated overall out-of-plane and in-plane success rates of 90% and 100%, respectively. The system and technique enable highly reproducible rotational control of single oocytes/embryos in three dimensions and pave the ground for automating a series of oocyte/embryo surgery tasks that require the targeting of specific cellular structures, such as the polar body.

References

[1] A. Nagy, M. Gertsenstein, K. Vintersten, and R. Behringer, *Manipulating the Mouse Embryo—A Laboratory Manual*, 3rd ed. New York: Cold Spring Harbor Laboratory Press, 2003.

[2] P. Stein and R. M. Schultz, "ICSI in mouse," *Methods Enzymol*., vol. 476, pp. 251–262, 2010.

[3] N. Yoshida and A. C. F. Perry, "Piezo-actuated mouse intracytoplasmic sperm injection (ICSI)," *Nat. Protoc*., vol. 2, no. 2, pp. 296–304, 2007.

[4] L. A. J. Van der Westerlaken, F. M. Helmerhorst, J. Hermans, and N. Naatgeboreen, "Intracytoplasmic sperm injection: Position of the polar body affects pregnancy rate," *Hum. Reprod*., vol. 14, no. 10, pp. 2565–2569, 1999.

[5] L. Gianaroli, "Preimplantation genetic diagnosis: Polar body and embryo biopsy," *Hum. Reprod*., vol. 15, no. 4, pp. 69–75, 2000.

[6] P. Braude, S. Pickering, F. Flinter, and C. M. Ogilvie, "Preimplantation genetic diagnosis," *Nat. Rev. Genet*., vol. 3, pp. 941–955, 2002.

[7] Y. Sun and B. J. Nelson, "Biological cell injection using an autonomous microrobotic system," *Int. J. Robot. Res*., vol. 21, no. 10–11, pp. 861–868, 2002.

[8] W. H. Wang, X. Y. Liu, and Y. Sun, "High-throughput automated injection of individual biological cells," *IEEE Trans. Autom. Sci. Eng*., vol. 6, no. 2, pp. 209–219, Apr. 2009.

[9] Z. Lu, X. Zhang, C. Leung, N. Esfandiari, R. Casper, and Y. Sun, "Robotic ICSI (intracytoplasmic sperm injection)," *IEEE Trans. Biomed. Eng*., vol. 58, no. 7, pp. 209–219, Jul. 2011.

[10] C. Leung, Z. Lu, N. Esfandiari, R. F. Casper, and Y. Sun, "Automated sperm immobilization for intracytoplasmic sperm injection," *IEEE Trans. Biomed. Eng*., vol. 58, no. 4, pp. 935–942, Apr. 2011.

[11] H. Lee, Y. Liu, D. Ham, and R. M. Westervelt, "Integrated cell manipulation system—CMOS/microfluidic hybrid," *Lab. Chip*, vol. 7, no. 3, pp. 331–337, 2007.

[12] S. Kobel, A. Valero, J. Latt, P. Renaud, and M. Lutolf, "Optimization of microfluidic single cell trapping for long-term on-chip culture," *Lab. Chip*, vol. 10, no. 7, pp. 857–863, 2010.

[13] T. Arakawa, M. Noguchi, K. Sumitomo, Y. Yamaguchi, and S. Shoji, "High-throughput single-cell manipulation system for a large number of target cells," *Biomicrofluidics*, vol. 5, no. 1, 014114, 2011.

[14] S. Bayoudh, T. A. Nieminen, N. R. Heckenberg, and H. Rubinsztein-Dunlop, "Orientation of biological cells using plane-polarized gaussian beam optical tweezers," *J. Mod. Opt*., vol. 50, no. 10, pp. 1581–1590, 2003.

[15] Y. Liu and M. Yu, "Investigation of inclined dual-fiber optical tweezers for 3d manipulation and force sensing," *Opt. Exp*., vol. 17, no. 16, pp. 13 624–13 638, 2009.

[16] S. Sato, M. Ishigure, and H. Inaba, "Optical trapping and rotational manipulation of microscopic particles and biological cells using higher-order mode nd:Yag laser beams," *Electron. Lett*., vol. 27, no. 20, pp. 1831–1832, 1991.

[17] M. Ichikawa, K. Kubo, K. Yoshikawa, and Y. Kimura, "Tilt control in optical tweezers," *J. Biomed. Opt*., vol. 13, no. 1, p. 101503, 2008.

[18] Y. L. Liang, Y. P. Huang, Y. S. Lu, M. T. Hou, and J. A. Yeh, "Cell rotation using optoelectronic tweezers," *Biomicrofluidics*, vol. 4, no. 4, 2010.

[19] M. C. Wu, "Optoelectronic tweezers," *Nat. Photon*., vol. 5, pp. 322–324, 2011.

[20] A. D. Goater and R. Pethig, "Electrorotation and dielectrophoresis," *Parasitology*, vol. 117, no. 7, pp. 177–189, 1999.

[21] M. Nishioka, S. Katsura, K. Hirano, and A. Mizuno, "Evaluation of cell characteristics by step-wise orientational rotation using optoelectrostatic micromanipulation," *IEEE Trans. Ind. Appl*., vol. 33, no. 5, pp. 1381–1388, Sep./Oct. 1997.

[22] R. Kunikata, Y. Takahashi, M. Koide, T. Itayama, T. Yasukawa, H. Shiku, and T. Matsue, "Three dimensional microelectrode array device integrating multi-channel microfluidics to realize manipulation and characterization of enzyme-immobilized polystyrene beads," *Sens. Actuators B, Chem*., vol. 141, no. 1, pp. 256–262, 2009.

[23] J. Park, S. W. Jung, Y. H. Kim, B. Kim, S. K. Lee, B. Ju, and K. I. Lee, "An integrated bio cell processor for single embryo cell manipulation," in *Proc. IEEE RSJ Int. Conf. Intell. Robots Syst*., Sendai, Japan, 2004, pp. 242–247.

[24] D. S. Gray, J. L. Tan, J. Voldman, and C. S. Chen, "Dielectrophoretic registration of living cells to a microelectrode array," *Biosens. Bioelectron*., vol. 19, no. 7, pp. 771–780, 2004.

[25] M. Ogiue-Ikeda and S. Ueno, "Magnetic cell orientation depending on cell type and cell density," *IEEE Trans. Magn*., vol. 40, no. 4, pp. 3024–3026, Jul. 2004.

[26] Y. Eguchi, M. Ogiue-Ikeda, and S. Ueno, "Control of orientation of rat schwann cells using an 8-T static magnetic field," *Neurosci. Lett*., vol. 351, no. 2, pp. 130–132, 2003.

[27] X. Liu, Z. Lu, and Y. Sun, "Orientation control of biological cells under inverted microscopy," *IEEE ASME Trans. Mechatron*., vol. 16, no. 5, pp. 918–924, Oct. 2011.

[28] D. F. Rogers, *Laminar Flow Analysis*. Cambridge, U.K.: Cambridge Univ. Press, 1992.

[29] D. Pnueli and C. Gutfinger, *Fluid Mechanics*. Cambridge, U.K.: Cambridge Univ. Press, 1997.

[30] N. Otsu, "Threshold selection method from gray-level histograms," *IEEE Trans. Syst. Man Cybern*., vol. 9, no. 1, pp. 62–66, Jan. 1979.

[31] M. W. Spong, S. Hutchinson, and M. Vidyasagar, *Robot Modeling and Control*. New York: Wiley, 2006, pp. 214–215.

Authors' photographs and biographies not available at the time of publication.